Contents lists available at ScienceDirect

Journal of the Mechanics and Physics of Solids

journal homepage: www.elsevier.com/locate/jmps

Diffusion-driven swelling-induced instabilities of hydrogels

Berkin Dortdivanlioglu, Christian Linder*

Department of Civil and Environmental Engineering, Stanford University, Stanford, CA 94305, USA

ARTICLE INFO

ABSTRACT

Under a variety of external stimuli, hydrogels can undergo coupled solid deformation and fluid diffusion and exhibit large volume changes. The numerical analysis of this process can be complicated by numerical instabilities when using mixed formulations due to the violation of the inf-sup condition. In addition, the large deformations produce complex instability patterns causing singularities in the underlying set of equations. For these reasons, the experimentally observed complex patterns remain elusive and poorly understood. Furthermore, a stability criterion suitable to detect critical conditions and predict post-instability patterns is lacking for hydrogel simulations. Here we investigate the stability criterion for coupled problems with a saddle point nature and propose a generic framework to study diffusion-driven swelling-induced instabilities of hydrogels. Adopting a numerically stable subdivision-based mixed isogeometric analysis, we show that the proposed framework for stability analysis accurately captures instability points during the transient swelling of hydrogels. The influence of geometrical and material parameters on the critical conditions are also presented in stability diagrams for two useful problems involving the buckling of hydrogel rods and the wrinkling on the surface of hydrogel bilayers. The results show that the short-time response of hydrogels immersed in water are highly unstable. We believe that this generic scheme provides a theoretical and computational foundation to study the morphogenesis in nature, and it also paves the way to create functional materials and design novel hydrogel devices through stability diagrams.

© 2018 Elsevier Ltd. All rights reserved.

1. Introduction

In general, hydrogels are polymer networks swollen due to diffusion of water. They exhibit large deformations in response to environmental changes in temperature, chemicals, electric fields, pH, humidity, and light (Beebe et al., 2000; Suzuki and Tanaka, 1990; Tanaka et al., 1980; 1982). Not only are they responsive materials but they are also soft, hydrophilic, and biocompatible (Li and Mooney, 2016). Because of these particular properties, hydrogels are adopted in diverse applications including actuators (Ionov, 2014), sensors (Buenger et al., 2012), responsive coatings (Holmes and Crosby, 2007), and drug delivery and bioadhesives (Peppas et al., 2006; Qiu and Park, 2001), to name few. In applications and in experiments using hydrogels, large deformations are sometimes observed to result in geometrical instabilities as compressive stresses inside the hydrogel increase due to the diffusion-driven swelling. The resulting bulk and surface instabilities initiated in the form of buckling (Lee et al., 2010; Mora and Boudaoud, 2006; Takahashi et al., 2016), bamboo and bubble instabilities (Boudaoud and Chaïeb, 2003; Matsuo and Tanaka, 1992), fringe and fingering instabilities (Biggins et al., 2013; Lin et al., 2017), wrinkling

---

* Corresponding author.
  E-mail address: linder@stanford.edu (C. Linder).

(Guvendiren et al., 2010), creasing (Southern and Thomas, 1965; Tanaka, 1986; Trujillo et al., 2008; Yoon et al., 2010), and their evolution are observed in both engineered hydrogel systems and in their natural counterparts, i.e. biological tissues (Kuhl, 2016) and plant bodies (Liu et al., 2013). For example, see Dervaux and Amar (2012) for a review. A quantification of the effects of transient and localized swellings due to the diffusion of water on the stability of hydrogels paves the way to better understanding of the morphogenesis in nature and will allow controlling and tuning of desired deformation modes to design functional hydrogel devices.

In this work, we study the complex material behavior of hydrogels along with dissipative fluid transport phenomena and their structural stability under transient diffusion-driven swelling deformations. We model the coupling of solid displacements and fluid diffusion with a nonlinear continuum-mechanical response and develop a mixed isogeometric analysis (IGA) based on non-uniform rational B-splines (NURBS) (Cottrell et al., 2009; Hughes et al., 2005) to investigate the large deformations and emerging geometrical instabilities. For the numerical modeling, strongly coupled chemo-mechanical problems often require separate approximations of the solid displacements and the chemical potential as the primary field driving fluid diffusion (Bouklas et al., 2015; Chester and Anand, 2010; Doi, 2009; Hong et al., 2008; Liu et al., 2016; Lucantonio et al., 2013). As a restriction of mixed methods, this independent discretization of primary fields often results in numerical instabilities in the form of severe oscillations in the solution of chemical potential field, violating the Ladyzhenskaya-Babuška-Brezzi (LBB) or the inf-sup condition (Babuška, 1973; Brezzi, 1974). For example, in the standard finite element context, the popular stable Taylor-Hood family of elements with quadratic displacement and linear chemical potential field approximations is adopted in Bouklas et al. (2015) and Böger et al. (2017) for hydrogel modeling and a low order mixed element formulation based on enhanced assumed strain techniques is developed in Krischok and Linder (2016) for coupled displacement-diffusion problems. In terms of short time behavior as $t \to 0$, hydrogels are similar to fully incompressible or quasi-compressible elastic materials due to the lack of time for water to diffuse. In the case of elasticity, mixed methods are adopted to circumvent locking issues in the incompressible limit. These locking issues can be prevented by alternatives such as B-bar, F-bar (Elguedj et al., 2008), and enhanced strain methods (Cardoso and Cesar de Sa, 2012). However, for hydrogel formulations with a strongly coupled chemo-mechanical nature, the continuous fluid flow over element boundaries requires higher order interpolation of the chemical potential to satisfy the balance of mass within the computational domain. Due to this continuity requirement and also for accuracy reasons, the coupled discretization necessitate the use of higher order stable mixed methods for hydrogel problems.

Apart from the numerical instabilities related to independent approximation technique of the main fields, physical instabilities may arise due to the highly nonlinear material response and nonlinearities in the problem geometry related to the global boundary value problem. Based on the early theoretical works (Hill, 1957) and Biot (1965), the structural stability criterion in the theory of finite elastic bodies is directly related to the loss of uniqueness of the solution to boundary value problems. Using this stability criterion, the stability analysis of quasi-compressible and fully incompressible elastic materials are investigated using mixed finite elements in Auricchio et al. (2005, 2013) and Schröder et al. (2017). Similarly, the coupled hydrogel formulation of displacement and chemical potential fields gives rise to a saddle point problem resulting in an indefinite system of governing equations. In indefinite systems, the detection of the occurrence of structural instabilities and the associated patterns is computationally nontrivial (Schröder et al., 2017). The goal of this contribution is to study diffusion-driven swelling-induced instabilities of hydrogels by providing a structural stability criterion suitable for strongly coupled hydrogel problems with a saddle-point nature. Based on this stability criterion, we study two useful problems involving the buckling of slender hydrogel rods and the surface wrinkling in hydrogel bilayers and construct stability diagrams exploiting material and geometrical parameters for each problem.

This manuscript is organized as follows. Section 2 deals with the formulation of the theories and our methodology. We derive the weak form of the balance equations in Section 2.1 through a mixed variational potential for the coupled problem of standard diffusion in incompressible solid matrices accommodating polymeric gels. In Section 2.2, we specify the energy storage potential accounting for the elastic stretching and the mixing of polymer with solvent molecules and the dissipation potential for the prescription of the fluid flux. Section 2.3 motivates the mixed IGA discretization of the weak equations introduced in Section 2.1 based on a subdivision-stabilization to construct a numerically stable formulation. In Section 2.4, we develop a criterion for the structural stability of the chemo-mechano coupled problems with a saddle-point nature and discuss its theoretical aspects. Based on this criterion, we devise two methodologies to capture diffusion-driven swelling-induced instabilities of hydrogels based on the eigenvalue analysis on the global system of equations and its Schur complement. Section 3 verifies the proposed schemes for the structural stability analysis to detect the onset of instabilities and critical modes using two numerical examples involving the buckling of hydrogel rods and the surface wrinkling of hydrogel bilayers. We explore the critical conditions for instabilities for a broad range of geometric and material parameters and gather all the results in design diagrams for each example. Concluding remarks are given in Section 4.

2. Theory

2.1. Mixed variational formulation for finite elasticity coupled with diffusion

The solvent diffusion in elastic solids is formulated as a coupled three-field problem, characterized by the deformation field φ, the concentration field c (number of solvent molecules per unit volume in the reference state), and the chemical potential μ. Following Miehe et al. (2014), we construct a variational principle for the evolution of elasticity coupled with

the standard Fickian-type diffusion, where the time-discrete counterpart of the rate-type potential $\Pi(\dot{\boldsymbol{\varphi}}, \dot{c}, \dot{\mu})$ in the domain $\mathcal{B}$ reads

$$\Pi^{\Delta}(\boldsymbol{\varphi}, c, \mu) = \int_{\mathcal{B}} \hat{\pi}^{\Delta}(\nabla\boldsymbol{\varphi}, c, \mu, \nabla\mu) dV - \Pi_{\text{ext}}^{\Delta}(\boldsymbol{\varphi}, \mu) \tag{1}$$

in the interval $[t_n, t]$ with a step length $\Delta t = t - t_n$ where the current time step t and the previous time step t_n. The potential $\Pi_{\text{ext}}^{\Delta}(\boldsymbol{\varphi}, \mu)$ corresponding to the external contribution accounts for the mechanically applied traction $\bar{\boldsymbol{T}}$ on the surface $\partial\mathcal{B}_T$ and prescribed species flux $\bar{H}$ normal to the surface $\partial\mathcal{B}_H$ such that

$$\Pi_{\text{ext}}^{\Delta}(\boldsymbol{\varphi}, \mu) = \int_{\partial\mathcal{B}_T} \bar{\boldsymbol{T}} \cdot \boldsymbol{\varphi} \, dA - \int_{\partial\mathcal{B}_H} \mu \bar{H} \, dA . \tag{2}$$

The internal contribution accounts for the overall stored and dissipative response by the incremental potential per unit volume

$$\hat{\pi}^{\Delta}(\boldsymbol{F}, c, \mu, \mathbb{M}) = \hat{\psi}(\boldsymbol{F}, c) - \mu(c - c_n) - \Delta t \hat{\phi}(\mathbb{M}; \boldsymbol{F}_n, c_n) , \tag{3}$$

where $\hat{\psi}(\boldsymbol{F}, c)$ is the stored free energy function depending on the deformation gradient defined as $\boldsymbol{F} := \nabla\boldsymbol{\varphi}$ and the concentration c. The dissipation function $\hat{\phi}(\mathbb{M}; \boldsymbol{F}_n, c_n)$ depends on the negative material gradient of the chemical potential $\mathbb{M} := -\nabla\mu$ at the current time step.

The solution $\{\boldsymbol{\varphi}^*, c^*, \mu^*\}$ at the current time step t is determined as the saddle point of the incremental potential Π^{Δ} via the incremental three-field saddle point principle

$$\left\{\boldsymbol{\varphi}^*, c^*, \mu^*\right\} = \text{Arg}\left\{\inf_{\boldsymbol{\varphi}\in U} \inf_{c\in C} \sup_{\mu\in M} \Pi^{\Delta}(\boldsymbol{\varphi}, c, \mu)\right\} , \tag{4}$$

where $U = [H_{\hat{\varphi}}^1(\mathcal{B})]^d$, $C = L_2(\mathcal{B})$, and $M = H_{\hat{\mu}}^1(\mathcal{B})$ where d is the spatial dimension.

In what follows, we enforce the molecular incompressibility of hydrogels as a kinematic constraint by eliminating c from the potential Π^{Δ}, the free energy $\hat{\psi}(\boldsymbol{F}, c) = \psi(\boldsymbol{F})$, and the dissipation function $\hat{\phi}(\mathbb{M}; \boldsymbol{F}_n, c_n) = \phi(\mathbb{M}; \boldsymbol{F}_n)$. As commonly adopted in the literature, we regard both the polymeric network and the fluid solvent as incompressible. Hence the consequent kinematic constraint of the molecular incompressibility (Hong et al., 2008) is

$$J = 1 + \nu c, \text{ where } \quad J := \det(\boldsymbol{F}) . \tag{5}$$

Equivalently the rate-type counterpart of (5) is

$$\dot{J} = 1 + \nu\dot{c} \quad \text{and} \quad \frac{\nu(c - c_n)}{\Delta t} = \frac{J - J_n}{\Delta t} . \tag{6}$$

Hence, the incremental potential density $\pi^{\Delta}(\boldsymbol{\varphi}, c, \mu, \nabla\mu)$ recasts into the reduced form

$$\pi_{\text{red}}^{\Delta}(\boldsymbol{F}, \mu, \mathbb{M}) = \psi(\boldsymbol{F}) - \frac{\mu}{\nu}(J - J_n) - \Delta t\phi(\mathbb{M}; \boldsymbol{F}_n) . \tag{7}$$

The solution $\{\boldsymbol{\varphi}^*, \mu^*\}$ at time step t is the saddle point of the reduced potential

$$\left\{\boldsymbol{\varphi}^*, \mu^*\right\} = \text{Arg}\left\{\inf_{\boldsymbol{\varphi}\in U} \sup_{\mu\in M} \Pi_{\text{red}}^{\Delta}(\boldsymbol{\varphi}, \mu)\right\} . \tag{8}$$

Taking the first variation of the two-field potential $\Pi_{\text{red}}^{\Delta}(\boldsymbol{\varphi}, \mu)$, we derive the weak form of the governing equations as

$$D\Pi_{\text{red}}^{\Delta}[\delta\boldsymbol{\varphi}] = \int_{\mathcal{B}} \left[\left(\partial_{\boldsymbol{F}}\psi - \frac{\mu}{\nu}J\boldsymbol{F}^{-T}\right) : \delta\boldsymbol{F}\right] dV - \int_{\partial\mathcal{B}_T} \bar{\boldsymbol{T}} \cdot \delta\boldsymbol{\varphi} \, dA = 0 \tag{9}$$

and

$$D\Pi_{\text{red}}^{\Delta}[\delta\mu] = \int_{\mathcal{B}} \left\{-\frac{\delta\mu}{\nu}(J - J_n) - \Delta t \, \partial_{\mathbb{M}}\phi \cdot \delta\mathbb{M}\right\} dV + \int_{\partial\mathcal{B}_H} \delta\mu\bar{H} \, dA = 0 \tag{10}$$

for all $\delta\boldsymbol{\varphi} \in [H_0^1(\mathcal{B})]^d$ and $\delta\mu \in H_0^1(\mathcal{B})$. The balance of linear momentum (9) and the balance of mass (10) are formulated in terms of the stored free energy ψ and the dissipation function ϕ, which will be given in the next section.

2.2. Constitutive energy and dissipation functions

Without loss of generalization, we adopt a general form of the free energy density ψ accounting for the elastic stretching of polymer network and the mixing of polymer network and solvent molecules such that $\psi(\boldsymbol{F}) = \psi_{\text{el}}(\boldsymbol{F}) + \psi_{\text{mix}}(\boldsymbol{F})$. The Neo-Hookean type elastic response is

$$\psi_{\text{el}}(\boldsymbol{F}) = \frac{1}{2}Nk_BT(\boldsymbol{F} : \boldsymbol{F} - 2\ln(J) - 3) , \tag{11}$$

where N is the number of polymer chains per volume of the dry gel, k_B is the Boltzmann-constant, and T is the temperature. The free energy density due to mixing of the polymer network and the solvent molecules is Flory (1942) and Huggins (1942)

$$\psi_{\text{mix}}(\boldsymbol{F}) = -\frac{k_B T}{v}\left(vc\,\ln\left(1+\frac{1}{vc}\right) + \frac{\chi}{1+vc}\right) = -\frac{k_B T}{v}\left((J-1)\,\ln\left(\frac{J}{J-1}\right) + \frac{\chi}{J}\right),\tag{12}$$

where v is the volume of a solvent molecule and χ is a dimensionless interaction parameter accounting for the enthalpy of mixing. We assume the following form for the dissipation function

$$\phi(\mathbb{M};\boldsymbol{F}_n) = \frac{c_n\,D}{2\,k_B T}\,\|\mathbb{m}\|^2 = \frac{(J_n-1)\,D}{2v\,k_B T}\,\|\mathbb{m}\|^2,\tag{13}$$

where D is the diffusivity, $\mathbb{m} = -\nabla_{x,n}\,\mu = \boldsymbol{F}_n^{-T}\mathbb{m}$ denotes the negative spatial gradient of the chemical potential, and the norm of a vector is defined as $\|\mathbb{m}\| = \sqrt{\mathbb{m}\cdot\mathbb{m}}$. Substituting the free energy density and the dissipation function into the governing equations; balance of linear momentum (9) and balance of mass (10) yields

$$\int_{\mathcal{B}}[\boldsymbol{\tau}:\nabla_{\boldsymbol{x}}^s\delta\boldsymbol{\varphi}]\,dV - \int_{\partial\mathcal{B}_T}\bar{\boldsymbol{T}}\cdot\delta\boldsymbol{\varphi}\,dA = 0\tag{14}$$

and

$$\int_{\mathcal{B}}\left\{-\frac{\delta\mu}{v}(J-J_n) - \Delta t\,\hat{\boldsymbol{q}}\cdot\delta\mathbb{m}\right\}dV + \int_{\partial\mathcal{B}_H}\delta\mu\bar{H}\,dA = 0.\tag{15}$$

where the first Piola Kirchhoff stress $\boldsymbol{\tau} = [\partial_{\boldsymbol{F}}\psi_{\text{el}} + \partial_{\boldsymbol{F}}\psi_{\text{mix}}]\boldsymbol{F}^T - \frac{\mu}{v}J\boldsymbol{1}$ and the Kirchhoff type flux vector $\hat{\boldsymbol{q}} = \partial_{\mathbb{m}}\phi = \frac{(J_n-1)D}{vk_B T}\mathbb{m}$. Recalling (12) and (11), the first Piola Kirchhoff stress can be derived as

$$\boldsymbol{\tau} = Nk_B T(\boldsymbol{b}-\boldsymbol{1}) + \frac{k_B T}{v}\left(J\,\ln\left(\frac{J-1}{J}\right) + \frac{\chi}{J} + 1\right)\boldsymbol{1} - \frac{\mu}{v}J\boldsymbol{1}.\tag{16}$$

Due to the term $\ln(J-1)$, numerical difficulties arise as $J\to 1$. In order to prevent this complication, we assume a pre-swollen stress-free initial state with the isotropic prestretch λ_0 (Chester and Anand, 2010; Hong et al., 2009a). In this initial state the hydrogel is in equilibrium with the homogeneous chemical potential μ^0 within the computational domain. Finally, the weak form (14) and (15) of the governing equations are discretized using separate approximations for the displacements and the chemical potential using a mixed isogeometric approach.

2.3. Mixed isogeometric analysis

In this section, we briefly introduce the B-splines and the subdivision-stabilization technique along with their utilization in mixed IGA. Consider a sequence of $n+p+1$ monotonically increasing equidistant numbers forming a uniform knot vector $\Xi = \{\xi_1, \xi_2, \ldots, \xi_{n+p+1}\}$, where p is the polynomial order and n is the number of basis functions and also the number of control points. Each knot ξ_i corresponds to a coordinate in the parameter space and they subdivide the parameter space into elements. Using this knot vector Ξ, uniform B-spline basis functions are formed recursively starting with the zeroth order B-splines (Cottrell et al., 2009; Piegl and Tiller, 1997) using

$$N_i^0(\xi) = \begin{cases} 1 & \text{if}\quad \xi_i \le \xi < \xi_{i+1} \\ 0 & \text{otherwise} \end{cases}\tag{17}$$

and, for higher order B-spline basis functions $p > 0$

$$N_i^p(\xi) = \frac{(\xi - \xi_i)N_i^{p-1}(\xi)}{\xi_{i+p} - \xi_i} + \frac{(\xi_{i+p+1} - \xi)N_{i+1}^{p-1}(\xi)}{\xi_{i+p+1} - \xi_{i+1}}.\tag{18}$$

Notice that each basis function $N_i^p(\xi)$ is non-zero over a knot interval $\xi_i \le \xi < \xi_{i+p+1}$ and has $p-1$ continuous derivatives across the knots and equivalently across the element boundaries. This higher order continuity is a distinctive feature of the isogeometric analysis. A B-spline curve $\boldsymbol{C}(\xi)$ of polynomial order p in $\mathbb{R}^d$ is constructed as linear combinations of basis functions $N_i^p(\xi)$

$$\boldsymbol{C}(\xi) = \sum_{i=1}^{n}N_i^p(\xi)\boldsymbol{B}_i,\tag{19}$$

where $\boldsymbol{B}$ is the set of n control points with the ith row $\boldsymbol{B}_i \in \mathbb{R}^d$. Although control points are analogous to nodal coordinates in the standard finite element context, as another distinctive feature of isogeometric analysis, they do not conform to the physical geometry when the polynomial order is two or higher. To construct conforming curves at the ends, *open* knot
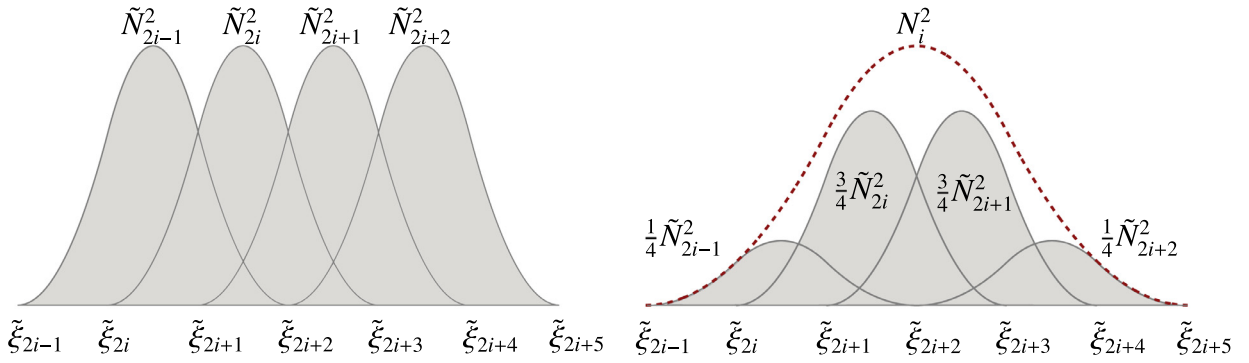
Fig. 1. The coarse basis functions are formed by linear combinations of $p+2$ fine shape functions. The coarse basis function $N_i^2 = \frac{1}{4}\tilde{N}_{2i-1}^2 + \frac{3}{4}\tilde{N}_{2i}^2 + \frac{3}{4}\tilde{N}_{2i+1}^2 + \frac{1}{4}\tilde{N}_{2i+2}^2$ for $p=2$.

vectors are adopted. *Open* knot vectors are formed by repeating the initial and final knot values $p+1$ times, i.e. $\xi_1 = \xi_2 = \ldots = \xi_{p+1}$ and $\xi_{n+1} = \ldots = \xi_{n+p} = \xi_{n+p+1}$. For the knots at the ends, their multiplicity becomes $k = p+1$. A pth order B-spline curve formed using a uniform open knot vector exhibits C^{p-1} continuity over the whole domain and $C^{p-k} = C^{-1}$ continuity at the ends. For further details on the B-splines and their continuity properties, see Cottrell et al. (2009) and Piegl and Tiller (1997).

Let us now consider one of the important features of B-splines which is the *two-scale* relation (Rüberg and Cirak, 2012; Zorin and Schröder, 2000). For any polynomial degree p, this relation is given by

$$N_i^p(\xi) = \frac{1}{2^p} \sum_{k=0}^{p+1} \binom{p+1}{k} \tilde{N}_{2i+k-1}^p(\xi) \ . \qquad \text{Equivalently that} \qquad \boldsymbol{N}^p(\boldsymbol{\xi}) = \boldsymbol{S} \, \tilde{\boldsymbol{N}}^p(\boldsymbol{\xi}) \ , \qquad (20)$$

where $\boldsymbol{S}$ is referred to as the subdivision matrix with the entries $S_k^p = \frac{1}{2^p}\binom{p+1}{k}$. The basis functions $\boldsymbol{N}^p$ are formed using a monotonically increasing uniform knot vector Ξ with the knot span h. Whereas, the basis function $\tilde{\boldsymbol{N}}^p$ is constructed by halving the knot intervals in Ξ, resulting in a finer basis with the knot span $h/2$. Overall, the *two-scale* relation (20) is used to form the coarse basis functions $\boldsymbol{N}^p$ via linear combinations of the fine basis functions $\tilde{\boldsymbol{N}}^p$. Figure 1 illustrates that the coarse basis functions N_i^p can be constructed by combining only $p+2$ fine basis functions $\tilde{N}_i^p$, scaled by the subdivision factors for $p=2$.

Extending the *two-scale* relation to NURBS, one-dimensional NURBS basis functions R_i^p can be constructed from B-spline functions (17) and (18) using

$$R_i^p(\xi) = \frac{N_i^p(\xi) \, w_i}{\sum_{i=1}^n N_i^p(\xi) \, w_i} \ , \qquad (21)$$

where w_i is the weight of the corresponding control point $\boldsymbol{B}_i$. The coarse and fine B-spline basis functions N_i^p and $\tilde{N}_i^p$ can be used to construct the NURBS functions in (21). Furthermore, surface NURBS functions and volume NURBS functions can be derived via the tensor products

$$
\begin{aligned}
R_{i,j}^{p,q} \qquad (\xi, \eta) &= \frac{N_i^p(\xi) \, N_j^q(\eta) \, w_{ij}}{\sum_{i=1}^n \sum_{j=1}^m N_i^p(\xi) \, N_j^q(\eta) \, w_{ij}} \text{ and} \\
R_{i,j,k}^{p,q,r} \quad (\xi, \eta, \zeta) &= \frac{N_i^p(\xi) \, N_j^q(\eta) \, N_k^r(\zeta) \, w_{ijk}}{\sum_{i=1}^n \sum_{j=1}^m \sum_{k=1}^l N_i^p(\xi) \, N_j^q(\eta) \, N_k^r(\zeta) \, w_{ijk}} .
\end{aligned}
\qquad (22)
$$

The corresponding knot vectors are $\Xi = \{\xi_1, \xi_2, \ldots, \xi_{n+p+1}\}$, $\mathcal{H} = \{\eta_1, \eta_2, \ldots, \eta_{m+q+1}\}$, and $\mathcal{Z} = \{\zeta_1, \zeta_2, \ldots, \zeta_{l+r+1}\}$ with the corresponding polynomial degrees p, q, and r.

The subdivision-stabilized mixed elements are proposed for fluid mechanics problems in Rüberg and Cirak (2012) and studied and demonstrated to satisfy the numerical inf-sup condition for strongly coupled displacement-diffusion problems in Dortdivanlioglu et al. (2018). This technique exploits the higher order continuity unique to isogeometric analysis for both the displacement and the chemical potential approximations. Compared with other available mixed IGA techniques (Dortdivanlioglu et al., 2018), the subdivision-stabilization technique also facilitates higher regularity over the computational domain, promoting robustness, vastly improved accuracy per degrees-of-freedom, and exact representation of complex geometries (Auricchio et al., 2015; Dedè et al., 2012; Gómez et al., 2008; Lipton et al., 2010).

For the numerical examples in Section 3, separate approximation spaces are used for the displacement and the chemical potential fields. Particularly, we adopt the Q2$_{SD}$/Q2 subdivision-stabilized mixed NURBS discretization where the chemical potential field discretization is constructed by k-refining the coarsest mesh, achieving its highest regularity. Then, it is further

subdivided (*h*-refined) to obtain the displacement field discretization, preserving the order and the highest regularity within the domain. This subdivision-stabilized mixed NURBS combination satisfies the inf-sup condition and furnishes oscillation-free robust solutions for strongly coupled diffusion in deforming porous solids (Dortdivanlioglu et al., 2018). As the main focus of this paper is on the structural instabilities in coupled hydrogel problems, we emphasize that unstable numerical methods would result in erroneous solutions in the displacement/chemical potential fields and consequently fail to detect the expected instability behavior in problems.

2.4. Structural stability analysis of coupled chemo-mechanics

For structural stability analysis, we consider the second variation of the potential $\Pi_{,dd}^{\Delta}$ where $d = [\varphi, \mu]^T$ (Miehe et al., 2015; Schröder et al., 2017). First, the discretization of the weak equations (14) and (15) is performed by separate approximation spaces for the deformation map and the chemical potential using

$$\varphi^h = \widetilde{R}^p \varphi = \widetilde{R}^p (X + u) \quad \text{and} \quad \mu^h = R^p \mu, \tag{23}$$

where $\widetilde{R}^p$ and R^p are the fine and coarse NURBS approximation spaces, φ and μ are the control variables. Plugging the approximations (23) into $\Pi_{,dd}^{\Delta}$, we obtain the discrete counterpart of the second variation of the mixed potential

$$\Pi_{,dd}^{\Delta} \approx \delta u^T K_{uu} \Delta u + \delta u^T K_{u\mu} \Delta \mu + \delta \mu^T K_{\mu u} \Delta u - \delta \mu^T K_{\mu\mu} \Delta \mu, \tag{24}$$

where $\delta(\cdot)$ and $\Delta(\cdot)$ refers to the corresponding virtual and incremental control variables, respectively. Equivalently that

$$\approx \delta d^T K \Delta d = \begin{bmatrix} \delta u \\ \delta \mu \end{bmatrix}^T \begin{bmatrix} K_{uu} & K_{u\mu} \\ K_{\mu u} & -K_{\mu\mu} \end{bmatrix} \begin{bmatrix} \Delta u \\ \Delta \mu \end{bmatrix}, \tag{25}$$

where d is the global vector with the unknowns $u \in \mathbb{R}^n$ and $\mu \in \mathbb{R}^m$. Notice that the global assembled stiffness matrix K is indefinite due to the saddle point nature of the problem and it is symmetric as a consequence of the variational treatment. Notice that $K_{u\mu} = K_{\mu u}^T$ and K_{uu} and $K_{\mu\mu}$ are positive definite and symmetric. Based on the characteristics of the global stiffness matrix and its globally condensed counterpart, we devise two equivalent, but computationally different, methodologies to capture the instability point and the anticipated pattern as follows:

Method 1 We can write

$$K = \begin{bmatrix} 1 & K_{u\mu} K_{\mu\mu}^{-1} \\ 0 & 1 \end{bmatrix} \underbrace{\begin{bmatrix} S & 0 \\ 0 & -K_{\mu\mu} \end{bmatrix}}_{\widehat{K}} \begin{bmatrix} 1 & 0 \\ K_{\mu\mu}^{-1} K_{\mu u} & 1 \end{bmatrix}, \tag{26}$$

where the block matrix $S = K_{uu} + K_{u\mu} K_{\mu\mu}^{-1} K_{\mu u}$, referred to as the Schur complement of K_{uu} in K. This decomposition can be used to obtain an uncoupled system of governing equations leading to a condensed displacement based formulation. More importantly, the Schur complement S can be exploited to perform a standard eigenvalue analysis on the coupled formulation, see for example Schröder et al. (2017). In a structurally stable state, K_{uu} and $K_{\mu\mu}$ are positive definite resulting in a positive definite Schur complement S. At the onset of instability, the Schur complement S becomes singular. Hence, the smallest positive eigenvalue of S can be tracked to assess the structural stability and its characteristics can be exploited to predict the geometrical instability. In this method, we perform standard eigenvalue analysis on S. For a detailed discussion of eigenvalue analysis for classical displacement based finite element formulations, see Schröder et al. (2017), Javili et al. (2015) and Wriggers (2008); Dortdivanlioglu et al., 2017. However, as a major drawback in this method, Schur complement computations are memory intensive and computationally costly operations since it requires the inversion of a big sparse matrix $K_{\mu\mu}$ and generally the inverse of a sparse matrix is a completely full matrix.

Method 2 Alternatively, the eigenspace representation of the global stiffness matrix K reads

$$K = K_1 \lambda_1 \otimes \lambda_1 + K_2 \lambda_2 \otimes \lambda_2 + \cdots + K_{n+m} \lambda_{n+m} \otimes \lambda_{n+m} = \sum_{i=1}^{n+m} K_i \lambda_i \otimes \lambda_i, \tag{27}$$

where K_i and λ_i for $i = 1, 2, \ldots, (m+n)$ are the eigenvalues and the corresponding unit eigenvectors, respectively. For the indefinite matrix K, the number of positive eigenvalues ($K_i > 0$) is n and the number of negative eigenvalues ($K_i < 0$) is m. Let K_a to be the smallest eigenvalue *in magnitude* approaching zero and define the instability point exactly when K_a becomes zero. At the instability point, the associated eigenvector λ_a contains the anticipated critical pattern.

Consider the decomposition $K = LDL^T$ where L is a unit lower triangular matrix and D is a diagonal matrix. Based on the Sylvester's law of inertia and the matrix congruence (Golub and Loan, 2013; Sylvester, 1852), the congruent matrices K, D, and $\widehat{K}$ share the same number of positive (n^+), negative (n^-), and zero (n^0) eigenvalues, and they have the signature (n^+, n^-, n^0). For the coupled stiffness matrix K, the signature ($n, m, 0$) refers to a structurally stable state. In this method, a bisection algorithm can be applied to pinpoint the instability points by tracking the change in the signature of the global
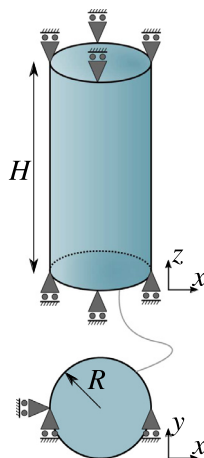
Fig. 2. Geometry and boundary conditions for the hydrogel rod problem. Both ends of the rod are free to slide in the $x - y$ plane. In addition, the rigid body motion is prevented by fixing the control point at $(-R, 0)$ in x and y directions and the control point at $(R, 0)$ in y direction on the bottom surface of the rod. The subdivision-stabilized $Q2_{SD}/Q2$ NURBS elements are adopted for the analysis of the problem.

stiffness matrix $\boldsymbol{K}$. The algorithm is terminated when the eigenvalue K_a related to the singularity is close to zero within a tolerance. Since we are only interested in a small subset in the eigenvalue spectrum of the real symmetric sparse matrix $\boldsymbol{K}$, efficient methods such as Arnoldi iterations can be used to compute the smallest eigenvalue *in magnitude*. In this method, the sparsity of the underlying system is preserved and exploited to render an efficient method.

Comparing both methods at the onset of instabilities, it can be shown that the critical eigenvector $\boldsymbol{\lambda}^{\alpha} \in \mathbb{R}^n$ of the Schur complement, i.e. $\boldsymbol{S}\boldsymbol{\lambda}^{\alpha} = \boldsymbol{0}$, emerges in the critical eigenvector $\boldsymbol{\lambda}_a = [\boldsymbol{\lambda}^{\alpha}, \boldsymbol{\lambda}^{\beta}]^T$ of the global stiffness matrix $\boldsymbol{K}$ where $\boldsymbol{\lambda}^{\beta} \in \mathbb{R}^m$. In the numerical examples, we also show that both methods capture the same critical instability points and patterns. Particularly, a non-standard eigenvalue analysis on the indefinite matrix $\boldsymbol{K}$ requires tracking of the smallest eigenvalue *in magnitude*. Whereas a standard eigenvalue analysis on $\boldsymbol{S}$ seeks the smallest positive eigenvalue to be negative or zero. Because hydrogels generally show extremely inhomogeneous and dynamic deformations in the short-time response (Wang et al., 2018), we emphasize that the stability of the structure should be assessed by tracking changes in the signature of the global stiffness matrix in order to render physical evolutions of the deformations.

3. Numerical examples

The objectives of this section are to verify the proposed scheme for the structural stability analysis to detect the onset of the instability and the critical pattern and also to provide stability diagrams accounting for the key geometrical and material parameters. This is done using two examples, the buckling of a three-dimensional hydrogel rod and wrinkling of a two-dimensional hydrogel bilayer. For the analysis, we adopt the equal order subdivision-stabilized $Q2_{SD}/Q2$ elements where the displacements $\boldsymbol{u}$ and the chemical potential field μ are both approximated by quadratic NURBS functions with the highest possible regularity, i.e. C^1, over the whole computational domain. It is worth emphasizing that the displacements are approximated on a fine mesh and the chemical potential is approximated on a coarse mesh although both NURBS functions have the same order and regularity. Otherwise, employing the same mesh for each field results in unstable numerical discretization. The standard Gauss quadrature rule with three points in each direction is employed.

3.1. Buckling of 3D slender hydrogel rod

3.1.1. Problem statement

In this example, we study the buckling of a swelling slender hydrogel rod with height H and radius R as shown in Fig. 2. We first construct the exact geometry using the coarsest discretization, i.e. a single quadratic NURBS element. This single element mesh is assigned to the chemical potential discretization. After constructing the displacement mesh through subdivision of the chemical potential mesh, both displacement and chemical potential discretizations are simultaneously h-refined for analysis purposes. In this way the highest possible regularity is achieved in the quadratic approximation spaces.

The material parameters for the hydrogel rod problem are as follows: $N\nu = 0.01$, the shear modulus $Nk_BT = 0.4$ MPa, and the interaction parameter $\chi = 0.1$. The diffusion constant is set to $D = 5 \times 10^{-3}$ mm^2/s. Initially, the hydrogel rod is in a stress-free equilibrium state with a free-swelling stretch of $\lambda_0 = 1.01$, which corresponds to the initial normalized chemical potential $\mu^0/k_BT = -2.461$. As the hydrogel rod is immersed in the solvent with a reference chemical potential $\mu^{ref} = 0$, the lateral surface of the rod is subjected to a sharp increase in the chemical potential. In the simulations, the initial chemical potential μ^0/k_BT is linearly increased to $\mu^{ref}/k_BT = 0$ in 1 s and later on it is kept constant. This chemical potential gradient
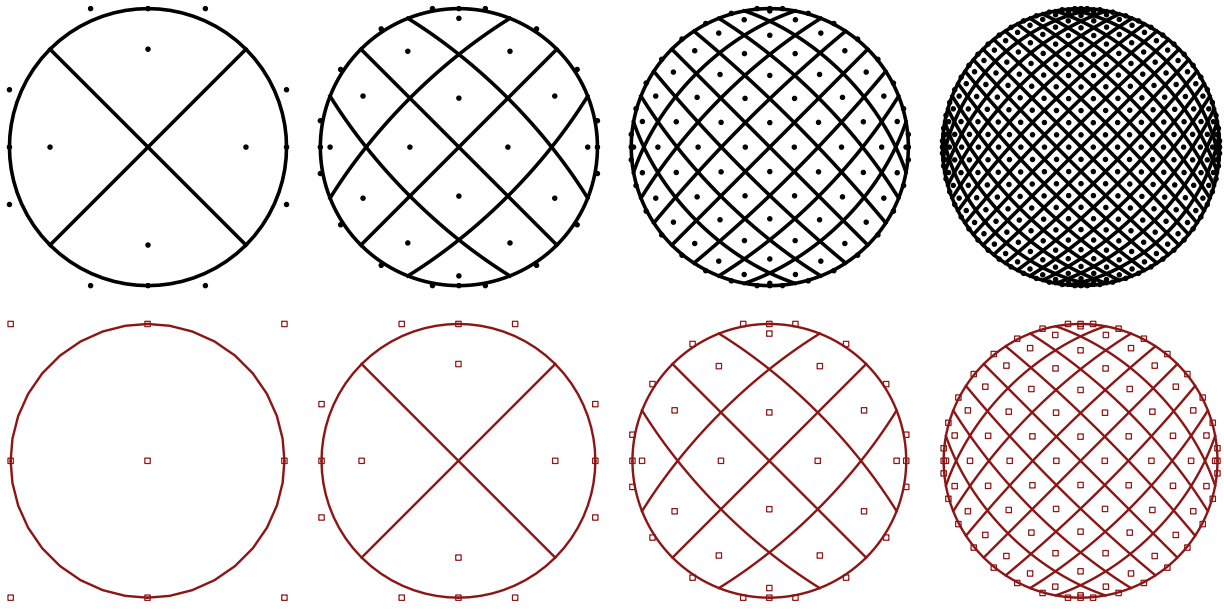
Fig. 3. Control net for displacement mesh (top row) and chemical potential mesh (bottom row) with $d_e = 2$, 4, 8, 16 subdivision-stabilized $Q2_{SD}/Q2$ mixed elements, respectively. Notice that d_e refers to the element number $d_e \times d_e$ of the displacement mesh in the cross-section. For clarity, only the cross-section mesh of 3D rod geometry is illustrated. A uniform mesh is applied over the height of the rod.

drives the diffusion process of water into the rod and consequently results in a transient swelling behavior of the hydrogel. The constraints at the rod ends result in compression in *z*-direction of the swelling rod. When this swelling force reaches a critical value, buckling of the slender rod is initiated.

3.1.2. Mesh convergence of critical chemical potential μ^c

In order to validate the performance of the proposed scheme to capture the critical chemical potential applied at the lateral surface, we perform a mesh convergence study. The number of elements corresponding to the displacement mesh are indicated by $d_e \times d_e \times h_e$, where $d_e \times d_e$ indicates the number of elements in the cross-section (see Fig. 3) and h_e indicates the number of elements along the height of the rod.

Figures 4A–C show the *h*-adaptive sensitivity analysis results for the critical chemical potential for different radii, $R = 0.05$, $R = 0.1$, and $R = 0.15$ (in mm) with varying mesh $d_e \times d_e \times h_e$. The convergence of the relative error in the critical chemical potential is plotted in Fig. 4D for increasing element number along the rod h_e, but constant element number $d_e = 30$ in the cross-section. Several conclusions can be drawn from the results in Fig. 4. First, increasing the number of elements d_e in the cross-section improves the results substantially. This is due to the localized chemical potential gradient close to the lateral surface where we prescribed a higher chemical potential as the boundary condition. Hence, in general it is recommended to have a finer mesh wherever the large strain gradients occur in the computational domain. Second, increasing the number of elements h_e along the rod more than $h_e = 24$ does not cause notable improvements in the results. And lastly, the convergence rate for the relative error in the critical chemical potential is algebraic for successive *h*-refinements.

3.1.3. Capturing the critical point and the buckling mode via eigenvalue analysis

In light of the convergence graph illustrated in Fig. 4, we employ the mesh $16 \times 16 \times 24$ that corresponds to the number of unknowns of 24620 and 896 for the displacements and the chemical potential, respectively. We perform an in-depth eigenvalue analysis study for the hydrogel rod with $R = 0.05$ mm by exploiting characteristics of both the Schur complement S and the global stiffness matrix K. Figure 5 A illustrates the trend of the eight smallest eigenvalues of the Schur complement S as the prescribed chemical potential on the boundary is increased over time. Simultaneously, we also track the change in the signature of the global stiffness matrix K, depicted in Fig. 5B.

This stability analysis study shows that the short time response of the gel is highly critical. The gel rod becomes unstable shortly after the chemical potential at the lateral surface started to increase. Further increase in the prescribed chemical potential leads multiple eigenvalues to become negative. We also show that the signature of K changes at the critical points and the same geometric instability pattern is predicted by the associated eigenvectors of K and S at each instability point, depicted in Fig. 6. The results suggest to perform stability analysis on the global stiffness matrix K instead of carrying out memory intensive Schur complement computations.
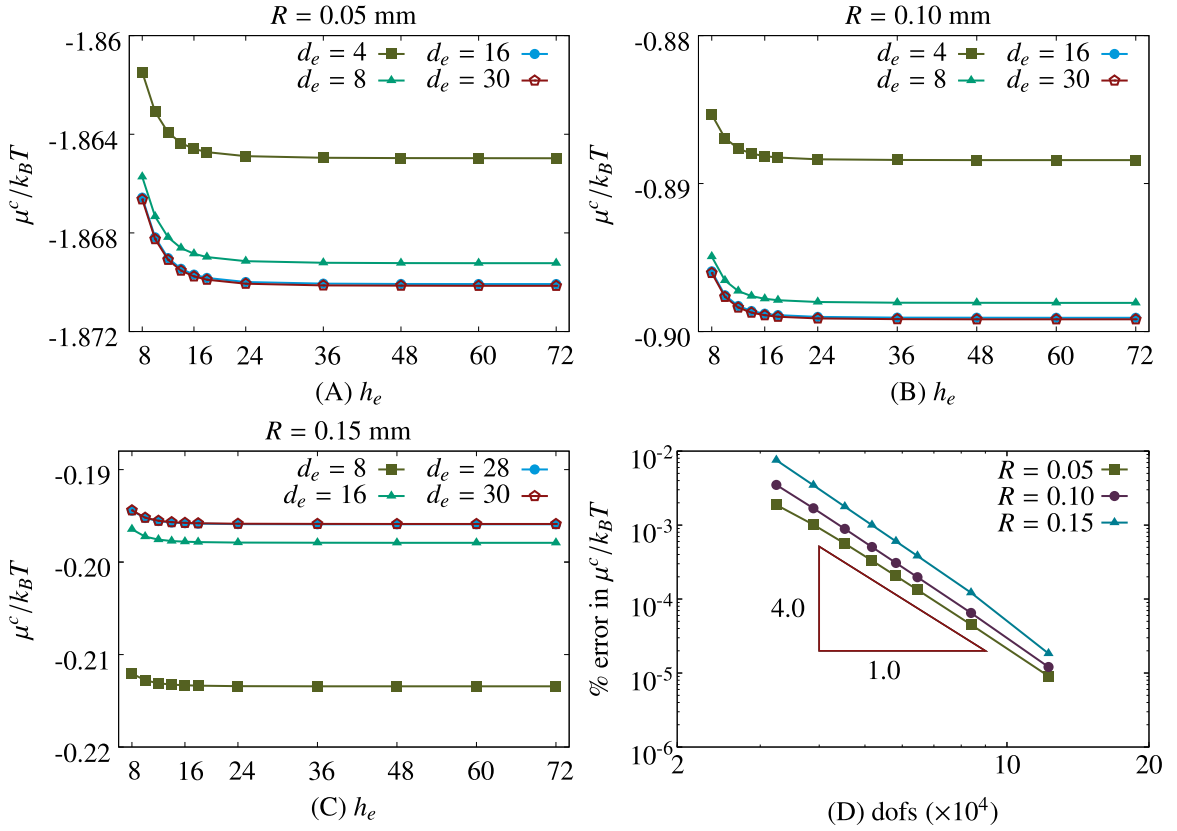
Fig. 4. Mesh convergence of critical chemical potential values at which buckling occurs for the hydrogel rod problem.
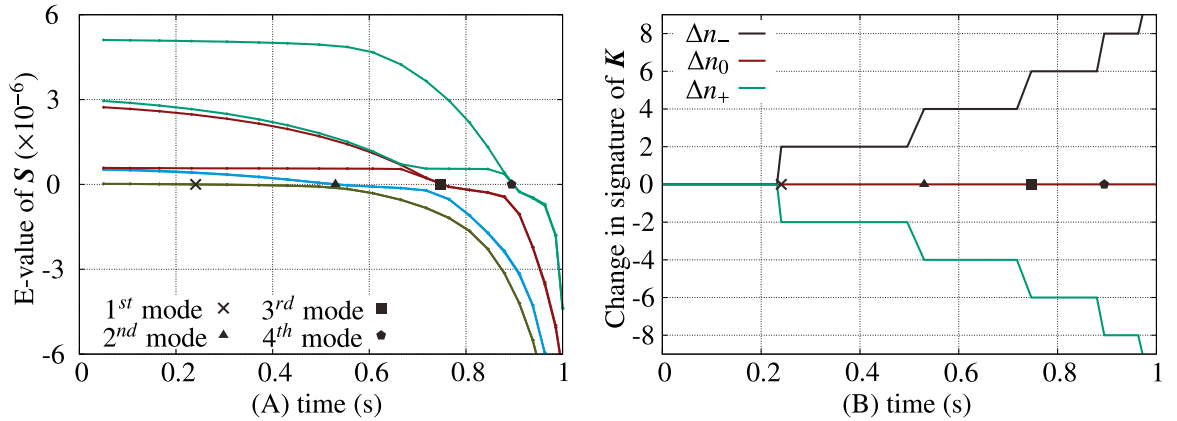

Fig. 5. *(A)* Trend of eigenvalues of the Schur complement S, *(B)* Change in the signature of the global stiffness matrix K.

3.1.4. Instability study and design diagrams of the hydrogel rod

In the previous section we have shown that a standard eigenvalue analysis on the Schur complement S successfully predicts the onset of the instability and its associated critical deformation mode. Equivalently, we have also identified the critical chemical potential and the geometric instability pattern by tracking the characteristics of the indefinite global stiffness matrix K.

In this section, we provide design diagrams revealing the critical conditions influenced by geometrical and material parameters to inform the design of hydrogel rods. For this purpose, we perform two useful studies.

We first investigate the influence of the radius R by varying it as $R = 0.05$, 0.1, 0.2, 0.3, 0.4 mm. For this part, we select the material parameters as in the previous examples. Figure 7 A shows the variation of the critical chemical potential as a function of the slenderness ratios, i.e. $2H/R$, for a given radius R. We can draw several conclusions from the results in Fig. 7A.

1st eigenmode 2nd eigenmode 3rd eigenmode 4th eigenmode
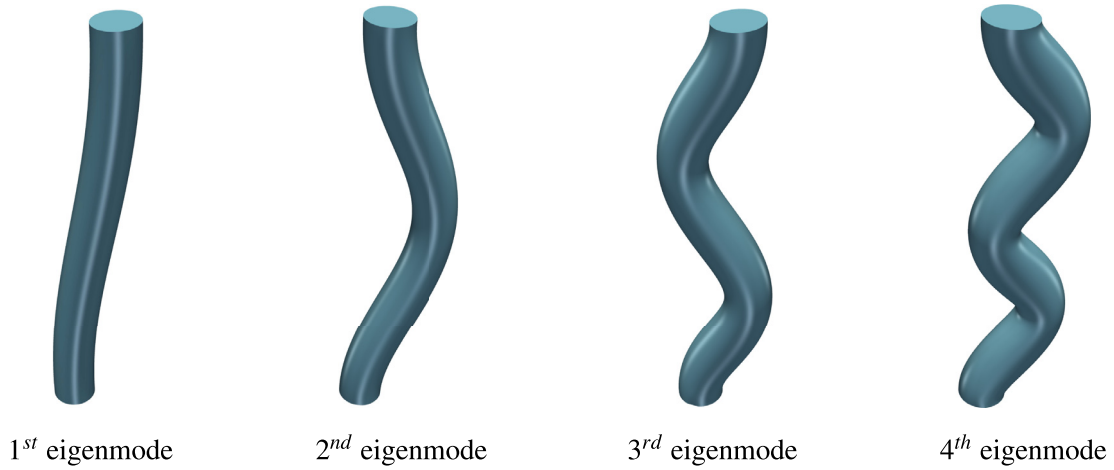
Fig. 6. First four critical eigenmodes associated with the critical swelling loads. The obtained modes are equivalent for both eigenvalue analysis approaches on $\boldsymbol{K}$ and $\boldsymbol{S}$.
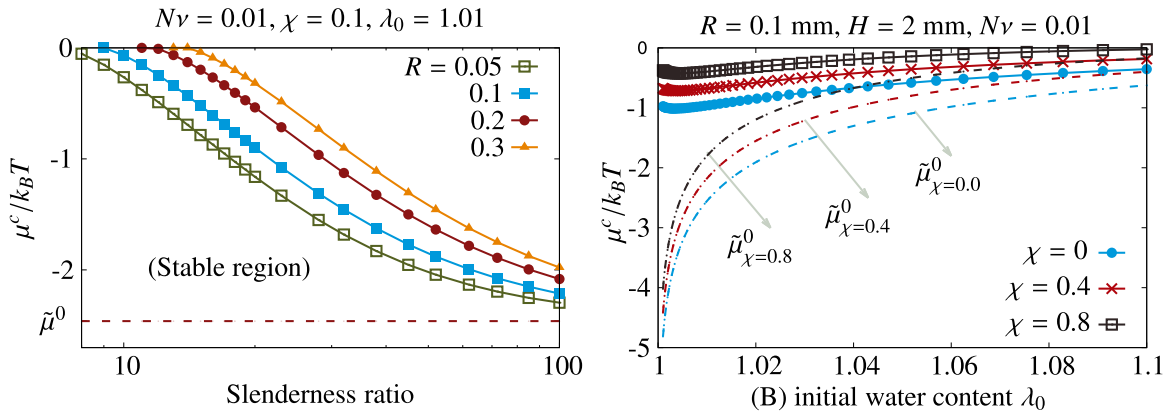

Fig. 7. (A) Critical chemical potential for buckling vs. the radius of the hydrogel rod. Notice that $\tilde{\mu}^0 = \mu^0/k_B T$. (B) Critical chemical potential vs. the dimensionless material parameters.

Firstly, for a given R, as the slenderness ratio increases, the buckling initiates earlier in time at a smaller critical chemical potential, resembling the behavior observed in classical beam buckling studies. Secondly, for a given slenderness ratio, we observed that the critical chemical potential increased when the radius of the hydrogel rod was increased. We anticipate that this response is due to the differential swelling starting at the lateral surface and progressing towards the center of the rod. This behavior results in swelling-induced stresses near the outer part of the cross-section and eventually increases the moment of inertia of the geometry with respect to the buckling plane. Finally, we observed that, for small slenderness ratios, the global buckling is no longer the dominant instability mode, which falls beyond the scope of this work.

For the second study, we analyze the influence of dimensionless material parameters $N\nu$, χ, and λ_0 on the stability of hydrogel rods with the radius of $R = 0.1$ mm and the height of $H = 2$ mm. As shown in Fig. 7B, hydrogel rods with higher initial water content buckled at higher chemical potentials and the critical chemical potential increases with increasing χ. Furthermore, the dimensionless parameter $N\nu$ does not have any significant influence on the investigated stability diagram of the hydrogel rod.

3.1.5. Post-buckling analysis of the hydrogel rod

In this section we perform post-buckling analysis of the hydrogel rod. Eigenvalue analysis only determines the onset of buckling and predicts the instability mode through characteristics of the stiffness matrix. In order to capture the actual deformation response and its evolution, we apply a stress-free initial deflection in the rod geometry as a slight perturbation to trigger the buckling. In particular, control points at $z = H$ are shifted by a deflection of 1% of the radius in the x-direction. Figure 8 presents the swollen configurations of the hydrogel rod with radius $R = 0.1$ mm and height $H = 1$, 2.5, 4 mm at time $t = 0$, 0.25, 0.63, 1, 3 s. The geometry is mirrored across the symmetry plane at $z = H$. The results in Fig. 8 demonstrate that tunable deformations can be obtained by controlling the chemical potential μ^{ref}, the geometry (R and H), and the material parameters (λ_0 and χ).
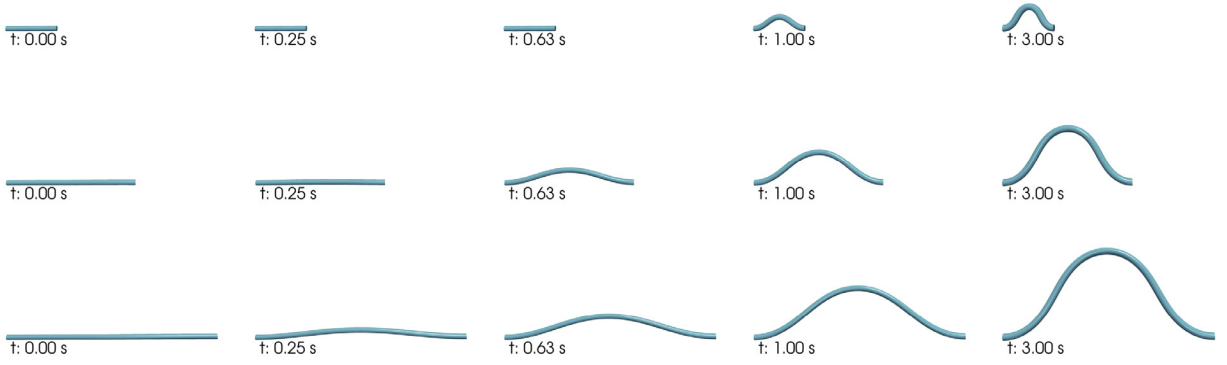
Fig. 8. The initial and the swollen configurations of the hydrogel rod with the radius $R = 0.1$ mm and the height $H = 1$ *(top row)*, 2.5 *(middle row)*, 4 mm *(bottom row)* at time $t = 0$, 0.25, 0.63, 1, 3 s.
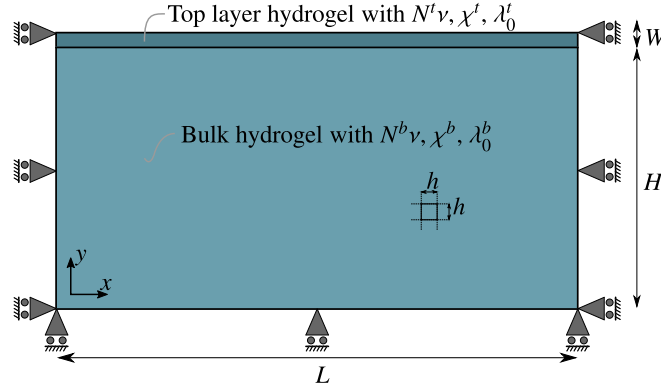

Fig. 9. Geometry and boundary conditions for the hydrogel bilayer problem. The geometry is formed using two separate patches starting with their coarsest discretization and connected with C^0 continuity at the interface.

3.2. Wrinkling of hydrogel bilayers

In this example, we study the wrinkling response of hydrogel bilayers with a larger shear modulus in the top layer compared to the shear modulus of the bulk hydrogel. Similar to wrinkle formation in elastomer bilayers, we observe a wrinkling response in hydrogel bilayers with a stiffer top layer.

3.2.1. Problem statement

The hydrogel bilayer is modeled as a two dimensional rectangular domain under plane strain conditions, constrained on the sides in the x-direction and at the bottom in the y-direction. This enforces symmetric boundary conditions on the sides. The top layer has thickness W with dimensionless material parameters $N^t v$, χ^t, and λ_0^t, and this top layer is perfectly bonded to the bulk hydrogel, which has height H and material parameters $N^b v$, χ^b, and λ_0^b.

The hydrogel bilayer makes contact with water on the top surface only. Notice that due to the adopted boundary conditions, hydrogel layers are swelling freely in the y-direction over time. In the simulations the chemical potential at the top surface is increased from $\mu^0/k_B T$ to the chemical potential of water $\mu^{ref}/k_B T = 0$ in 1 s.

3.2.2. Mesh convergence of critical chemical potential μ^c

In this section we perform an h-adaptive sensitivity analysis by varying the mesh size h and compute the critical chemical potential that triggers the wrinkling in the top hydrogel layer of Fig. 9 with length $L = 1$ mm, height $H = 1$ mm and top layer thickness $W = 0.05$ mm. The dimensionless material parameters are $N^b v = 10^{-4}$, $\chi^t = \chi^b = 0.1$, and $\lambda_0^b = \lambda_0^t = 1.01$, and we define the shear modulus ratio as N^t/N^b. The diffusion parameter is set to $D = 5 \times 10^{-3}$ mm^2/s.

Figures 10 A–C show that the accuracy in the critical chemical potential improves with increasing total degrees-of-freedom and Fig. 10D show the relative error with respect to the finest solution for the shear modulus ratios $N^t/N^b = 8$, 100, and 1000. We obtain an algebraic convergence in the error of critical chemical potential for the successive h-refinements as depicted in Fig. 10. However, the percent error in solutions for the ratio $N^t/N^b = 8$ are roughly three orders of magnitude larger compared to the percent error in the solutions for $N^t/N^b = 100$. This difference can be explained as follows. For the shear modulus ratio $N^t/N^b = 8$, the wrinkling instability is observed at considerably high critical chemical potential $\mu^c/k_B T = -0.09$ whereas the critical chemical potential $\mu^c/k_B T = -1.20$ for the shear modulus ratio $N^t/N^b = 100$. For
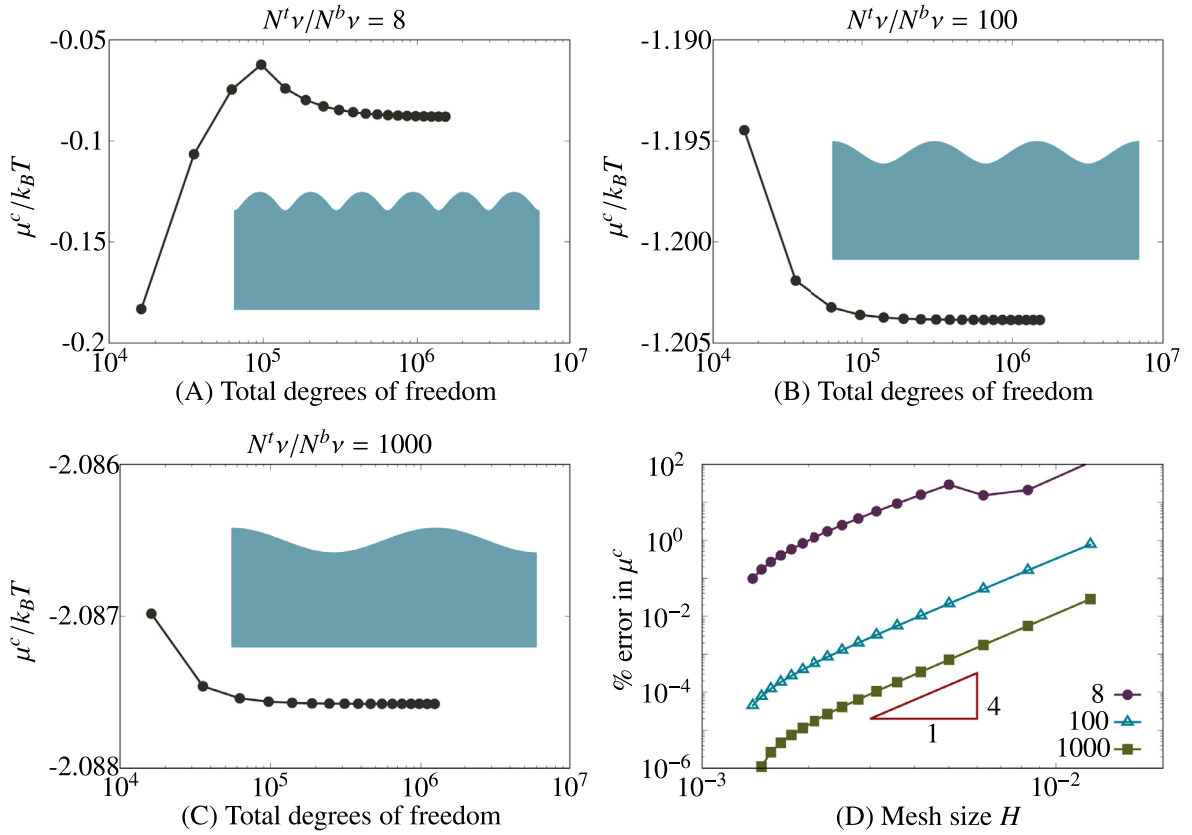
Fig. 10. Mesh convergence of critical chemical potential at which surface wrinkling is triggered for the hydrogel bilayer problem for the ratio $N^t/N^b = 8$ (A), 100 (B), 1000 (C). (D) Comparison of the relative percent error convergence for the critical chemical potential. The wrinkled configurations are not the actual deformations, but the critical eigenmodes of the converged solutions.

extremely large shear modulus ratios, the response of the bulk hydrogel against the film vanishes significantly. Hence, the bulk hydrogel plays a minor role for larger shear modulus ratios, resulting in more accurate solutions for the same degrees-of-freedom. We also observe a competition between short-wavelength and long-wavelength instabilities for small shear modulus ratios. For a detailed study on short-wavelength Biot-type instabilities in homogeneous hydrogels, see Kang and Huang (2010). For example, in Fig. 10A, the initial convergence of the critical chemical potential is towards the short-wavelength mode, but it switches to the long-wavelength mode as we further refine the mesh. When the ratio N^t/N^b is smaller than roughly eight, eigenmodes associated with the critical chemical potentials no longer predict long-wavelength instability modes. The wrinkled configurations illustrated in Fig. 10A–C correspond to the eigenmodes at the instability points.

3.2.3. Instability study and design diagrams of hydrogel bilayer

So far we have studied the mesh convergence of the critical chemical potential for the bilayer hydrogels with a thin and stiffer top layer and we have observed that the proposed scheme for stability analysis of coupled hydrogel problems serves as a powerful tool to study the wrinkle patterns and the critical conditions for their appearance. In this section we investigate the influence of the thickness of the top layer W, the dimensionless material parameters $N\nu$, χ, and λ_0, and the shear modulus ratio $N^t\nu/N^b\nu$ on the instability response of the bilayer system. The length is set to $L = 10$ mm to accommodate more wrinkles on the surface, and the height $H = 1$ mm.

Figure 11 A compares the critical chemical potential for varying shear modulus ratios in the range $N^t\nu/N^b\nu = [8, 1000]$ and for top layer thicknesses $W = 0.025, 0.05$, and 0.075 mm, whereas the corresponding number of wrinkles observed on the surface are illustrated in Fig. 11B. For simplicity, we keep the other material parameters constant at $N^b\nu = 10^{-4}$, $\chi^{b,t} = 0.1$, and $\lambda_0^{b,t} = 1.01$. This study results in following conclusions. First, for a given thickness W, increasing the shear modulus ratio reduces the critical chemical potential. Second, for a given shear modulus ratio, increasing the thickness W leads to the need for a larger critical chemical potential to initiate the wrinkling instability. Third, the lower limit of the shear modulus ratio for which we still observe wrinkling instability is increased as the thickness of the top layer is increased. Lastly, the number of wrinkles increases as both the shear modulus ratio and the thickness of the top layer decreases. These results can be explained by an optimization of the strain energy in the bilayer system due to the contributions of both the
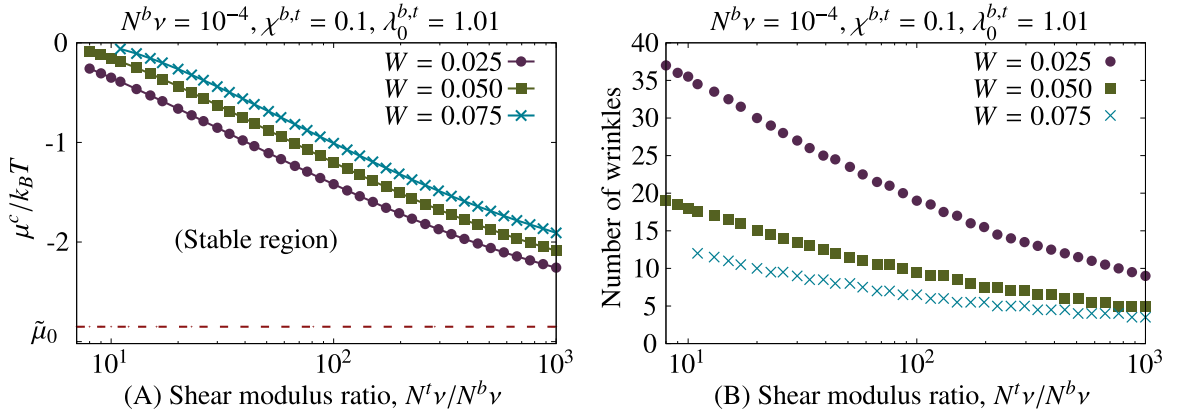
Fig. 11. Effect of thickness on the critical chemical potential and number of wrinkles. $L = 10$ mm, $H = 1$ mm.
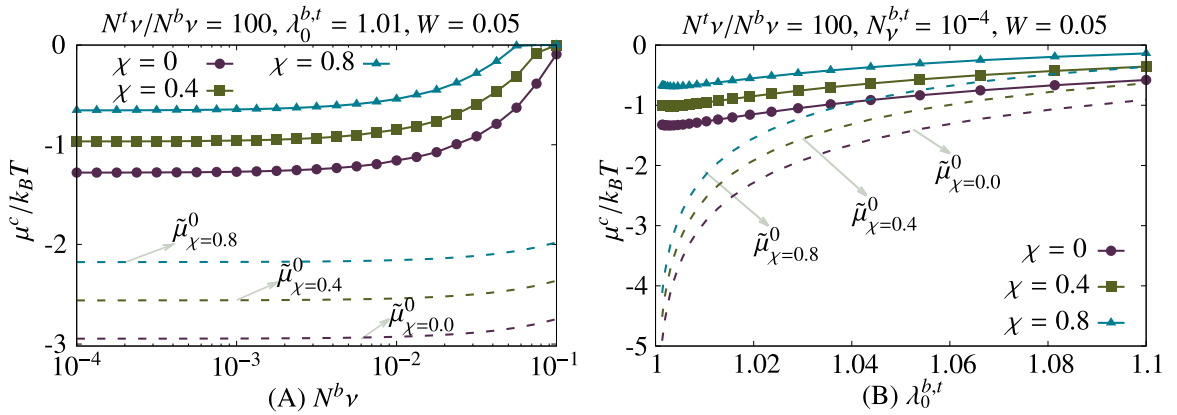

Fig. 12. (A) Influence of $N^b\nu$ and $\chi^{b,t}$ on the critical chemical potential. (B) Influence of $\lambda^{b,t}_0$ and $\chi^{b,t}$ on the critical chemical potential.

bending of the top hydrogel layer and the stretching in the bulk hydrogel. For small thicknesses of the top hydrogel layer, the bending of the top layer requires less energy compared to the bending of thicker samples. Therefore, more wrinkles are observed on the surface as the thickness decreases. Similarly, as the shear modulus ratio gets smaller for a given thickness of the top hydrogel layer, the energy due to stretching of the bulk hydrogel becomes more significant. Consequently, more wrinkles are observed on the surface as the shear modulus ratio decreases. Furthermore, the diffusion length plays an important role on the critical chemical potential for varying thickness values. Compared to the limit case where the film and the bulk hydrogels are swelling homogeneously, the diffusion phenomenon introduces a differential swelling response that starts at the top surface and reduces over the depth. This differential swelling results in an increase in the thickness of the top layer and rises the critical chemical potential.

Figure 12 illustrates the influence of the dimensionless material parameters $N^b\nu$, χ^b, and λ^b_0 on the critical chemical potential. Notice that we set the additional material parameters as $\chi^b = \chi^t$, $\lambda^b_0 = \lambda^t_0$, the thickness $W = 0.05$ mm, and the shear modulus ratio $N^t\nu/N^b\nu = 100$. As shown in Fig. 12A, the critical chemical potential is not influenced by the shear modulus of the bulk hydrogel when roughly $N^b\nu < 10^{-2}$. In this range ($N^b\nu < 10^{-2}$), the energy contribution due to the elastic stretching of polymeric network becomes negligible and the energy contribution due to the mixing of polymeric network with solvent molecules becomes dominant. This interplay between energetic contributions plays a critical role in the stability analysis. Therefore, the critical chemical potential highly depends on the interaction parameter χ. Figure 12B shows that a higher water content at the initial state of the hydrogel bilayer increases the critical chemical potential. In addition, we observe the interaction parameter χ and the shear modulus of the bulk hydrogel $N^b\nu$ for a given shear modulus ratio do not influence the number of wrinkles emerging on the surface of the bilayer (not presented due to redundancy).

4. Conclusion

In this work, we presented a criterion for the structural stability of hydrogels with strongly coupled diffusion based on the loss of uniqueness of the solution to the global boundary value problem. Based on this criterion, we showed that the onset of instabilities is associated with a singularity in the Schur complement of the global stiffness matrix which is

indefinite due to the saddle point nature of the problem. This concluded that the global stiffness matrix and its Schur complement share the same eigenvalue characteristics revealing the critical conditions for the instabilities. In doing so, we also proved the structural stability of hydrogels during the transient swelling by tracking the change in the signature of the global stiffness matrix. Together with the ability of IGA to exactly represent the geometry, numerically stable mixed isogeometric analysis based on subdivision-stabilization proved robustness in capturing the complex swelling behavior of hydrogels. For two numerical examples, the proposed computational scheme successfully predicted the critical patterns and the conditions on their emergence, as well as the post-buckling responses. In addition, stability diagrams predicting critical conditions for a broad range of geometric and material parameters were constructed for both the buckling problem of hydrogel rods and the wrinkling behavior of hydrogel bilayers. It was found that the short-time responses of hydrogels in both problems are highly unstable because of the localized swelling driven by the solvent diffusion. This work is expected to provide a theoretical guidance on the structural stability of hydrogels with strongly coupled diffusion and help design tunable deformations harnessing instabilities in hydrogel rods and bilayers. Apart from structural instabilities such as buckling and wrinkling, crease formation in gels are commonly observed in experiments and applications (Curatolo et al., 2017; Guvendiren et al., 2010; Hwa and Kardar, 1988; Jin et al., 2014; Takahashi et al., 2016). Creasing is a nonlinear material instability (Ciarletta, 2018), which is beyond the scope of the paper and a task for future investigations. However, the developed theoretical and numerical methods can be used to study the formation and dynamic evolution of these complex instability phenomena in gels (Hong et al., 2009b; Weiss et al., 2013).

Acknowledgements

References

Auricchio, F., Conti, M., Ferraro, M., Morganti, S., Reali, A., Taylor, R.L., 2015. Innovative and efficient stent flexibility simulations based on isogeometric analysis. Comput. Methods Appl. Mech. Eng. 295, 347–361.
Auricchio, F., Beirão da Veiga, L., Lovadina, C., Reali, A., 2005. A stability study of some mixed finite elements for large deformation elasticity problems. Comput. Methods Appl. Mech. Eng. 194 (9), 1075–1092.
Auricchio, F., Beirão da Veiga, L., Lovadina, C., Reali, A., Taylor, R.L., Wriggers, P., 2013. Approximation of incompressible large deformation elastic problems: some unresolved issues. Comput. Mech. 52 (5), 1153–1167.
Babuška, I., 1973. The finite element method with Lagrangian multipliers. Numerische Mathematik 20 (3), 179–192.
Beebe, D.J., Moore, J.S., Bauer, J.M., Yu, Q., Liu, R.H., Devadoss, C., Jo, B.-H., 2000. Functional hydrogel structures for autonomous flow control inside microfluidic channels. Nature 404, 588.
Biggins, J.S., Saintyves, B., Wei, Z., Bouchaud, E., Mahadevan, L., 2013. Digital instability of a confined elastic meniscus. Proc. Natl. Acad. Sci. USA 110 (31), 12545.
Biot, M.A., 1965. Mechanics of Incremental Deformations. John Wiley and Sons, New York.
Böger, L., Nateghi, A., Miehe, C., 2017. A minimization principle for deformation-diffusion processes in polymeric hydrogels: constitutive modeling and FE implementation. Int. J. Solids Struct. 121, 257–274.
Boudaoud, A., Chaïeb, S., 2003. Mechanical phase diagram of shrinking cylindrical gels. Phys. Rev. E 68 (2), 021801.
Bouklas, N., Landis, C.M., Huang, R., 2015. A nonlinear, transient finite element method for coupled solvent diffusion and large deformation of hydrogels. J. Mech. Phys. Solids 79, 21–43.
Brezzi, F., 1974. On the existence, uniqueness and approximation of saddle-point problems arising from Lagrangian multipliers. Revue française d'automatique, informatique, recherche opérationelle. 8 (2), 129–151.
Buenger, D., Topuz, F., Groll, J., 2012. Hydrogels in sensing applications. Prog. Polym. Sci. 37 (12), 1678–1719.
Cardoso, R.P.R., Cesar de Sa, J.M.A., 2012. The enhanced assumed strain method for the isogeometric analysis of nearly incompressible deformation of solids. Int. J. Numer. Methods Eng. 92 (1), 56–78.
Chester, S.A., Anand, L., 2010. A coupled theory of fluid permeation and large deformations for elastomeric materials. J. Mech. Phys. Solids 58 (11), 1879–1906.
Ciarletta, P., 2018. Matched asymptotic solution for crease nucleation in soft solids. Nat. Commun. 9 (1), 496.
Cottrell, J.A., Hughes, T.J.R., Bazilevs, Y., 2009. Isogeometric Analysis: Toward Integration of CAD and FEA, First Wiley Publishing.
Curatolo, M., Nardinocchi, P., Puntel, E., Teresi, L., 2017. Transient instabilities in the swelling dynamics of a hydrogel sphere. J. Appl. Phys. 122 (14), 145109.
Dedè, L., Borden, M.J., Hughes, T.J.R., 2012. Isogeometric analysis for topology optimization with a phase field model. Arch. Comput. Methods Eng. 19 (3), 427–465.
Dervaux, J., Amar, M.B., 2012. Mechanical instabilities of gels. Annu. Rev. Condens. Matter Phys. 3 (1), 311–332.
Doi, M., 2009. Gel dynamics. J. Phys. Soc. Jpn. 78 (5), 052001.
Dortdivanlioglu, B., Javili, A., Linder, C., 2017. Computational aspects of morphological instabilities using isogeometric analysis. Comput. Methods Appl. Mech. Eng. 316, 261–279.
Dortdivanlioglu, B., Krischok, A., Beirão da Veiga, L., Linder, C., 2018. Mixed isogeometric analysis of strongly coupled diffusion in porous materials. Int J Numer Methods Eng 114 (1), 28–46.
Elguedj, T., Bazilevs, Y., Calo, V.M., Hughes, T.J.R., 2008. F and B projection methods for nearly incompressible linear and non-linear elasticity and plasticity using higher-order NURBS elements. Comput. Methods Appl. Mech. Eng. 197 (33–40), 2732–2762.
Flory, P.J., 1942. Thermodynamics of high polymer solutions. J. Chem. Phys. 10 (1), 51–61.
Golub, G.H., Loan, C.F.V., 2013. Matrix Computations, Fourth The John Hopkins University Press, Baltimore.
Gómez, H., Calo, V.M., Bazilevs, Y., Hughes, T.J.R., 2008. Isogeometric analysis of the Cahn–Hilliard phase-field model. Comput. Methods Appl. Mech. Eng. 197 (49–50), 4333–4352.
Guvendiren, M., Burdick, J.A., Yang, S., 2010. Solvent induced transition from wrinkles to creases in thin film gels with depth-wise crosslinking gradients. Soft Matter 6 (22), 5795–5801.
Hill, R., 1957. On uniqueness and stability in the theory of finite elastic strain. J. Mech. Phys. Solids 5 (4), 229–241.
Holmes, D.P., Crosby, A.J., 2007. Snapping surfaces. Adv. Mater. 19 (21), 3589–3593.
Hong, W., Liu, Z., Suo, Z., 2009. Inhomogeneous swelling of a gel in equilibrium with a solvent and mechanical load. Int. J. Solids Struct. 46 (17), 3282–3289.
Hong, W., Zhao, X., Suo, Z., 2009. Formation of creases on the surfaces of elastomers and gels. Appl. Phys. Lett. 95 (11), 111901.

Hong, W., Zhao, X., Zhou, J., Suo, Z., 2008. A theory of coupled diffusion and large deformation in polymeric gels. J. Mech. Phys. Solids 56 (5), 1779–1793.

Huggins, M.L., 1942. Some properties of solutions of long-chain compounds. J. Phys. Chem. 46 (1), 151–158.

Hughes, T.J.R., Cottrell, J.A., Bazilevs, Y., 2005. Isogeometric analysis: CAD, finite elements, NURBS, exact geometry and mesh refinement. Comput. Methods Appl. Mech. Eng. 194 (39–41), 4135–4195.

Hwa, T., Kardar, M., 1988. Evolution of surface patterns on swelling gels. Phys. Rev. Lett. 61, 106–109.

Ionov, L., 2014. Hydrogel-based actuators: possibilities and limitations. Mater. Today 17 (10), 494–503.

Javili, A., Dortdivanlioglu, B., Kuhl, E., Linder, C., 2015. Computational aspects of growth-induced instabilities through eigenvalue analysis. Comput. Mech. 56, 405–420.

Jin, L., Chen, D., Hayward, R.C., Suo, Z., 2014. Creases on the interface between two soft materials. Soft Matter 10 (2), 303–311.

Kang, M.K., Huang, R., 2010. Swell-induced surface instability of confined hydrogel layers on substrates. J. Mech. Phys. Solids 58 (10), 1582–1598.

Krischok, A., Linder, C., 2016. On the enhancement of low-order mixed finite element methods for the large deformation analysis of diffusion in solids. Int. J. Numer. Methods Eng. 106 (4), 278–297.

Kuhl, E., 2016. Unfolding the brain. Nat. Phys. 12, 533.

Lee, H., Xia, C., Fang, N.X., 2010. First jump of microgel; actuation speed enhancement by elastic instability. Soft Matter 6 (18), 4342–4345.

Li, J., Mooney, D.J., 2016. Designing hydrogels for controlled drug delivery. Nat. Rev. Mater. 1, 16071.

Lin, S., Mao, Y., Radovitzky, R., Zhao, X., 2017. Instabilities in confined elastic layers under tension: fringe, fingering and cavitation. J. Mech. Phys. Solids 106, 229–256.

Lipton, S., Evans, J.A., Bazilevs, Y., Elguedj, T., Hughes, T.J.R., 2010. Robustness of isogeometric structural discretizations under severe mesh distortion. Comput. Methods Appl. Mech. Eng. 199 (5–8), 357–373.

Liu, Y., Zhang, H., Zhang, J., Zheng, Y., 2016. Transient swelling of polymeric hydrogels: a new finite element solution framework. Int. J. Solids Struct. 80, 246–260.

Liu, Z., Swaddiwudhipong, S., Hong, W., 2013. Pattern formation in plants via instability theory of hydrogels. Soft Matter 9 (2), 577–587.

Lucantonio, A., Nardinocchi, P., Teresi, L., 2013. Transient analysis of swelling-induced large deformations in polymer gels. J. Mech. Phys. Solids 61 (1), 205–218.

Matsuo, E.S., Tanaka, T., 1992. Patterns in shrinking gels. Nature 358, 482.

Miehe, C., Mauthe, S., Ulmer, H., 2014. Formulation and numerical exploitation of mixed variational principles for coupled problems of cahn-Hilliard-type and standard diffusion in elastic solids. Int. J. Numer. Methods Eng. 99 (10), 737–762.

Miehe, C., Vallicotti, D., Zäh, D., 2015. Computational structural and material stability analysis in finite electro-elasto-statics of electro-active materials. Int. J. Numer. Meth. Eng. 102 (10), 1605–1637.

Mora, T., Boudaoud, A., 2006. Buckling of swelling gels. Eur. Phys. J. E 20 (2), 119–124.

Peppas, N.A., Hilt, J.Z., Khademhosseini, A., Langer, R., 2006. Hydrogels in biology and medicine: from molecular principles to bionanotechnology. Adv. Mater. 18 (11), 1345–1360.

Piegl, L., Tiller, W., 1997. The NURBS Book, Second Springer, Berlin.

Qiu, Y., Park, K., 2001. Environment-sensitive hydrogels for drug delivery. Triggering Drug Delivery Syst. 53 (3), 321–339.

Rüberg, T., Cirak, F., 2012. Subdivision-stabilised immersed b-spline finite elements for moving boundary flows. Comput. Methods Appl. Mech. Eng. 209–212, 266–283.

Schröder, J., Viebahn, N., Wriggers, P., Auricchio, F., Steeger, K., 2017. On the stability analysis of hyperelastic boundary value problems using three- and two-field mixed finite element formulations. Comput. Mech. 60 (3), 479–492.

Southern, E., Thomas, A.G., 1965. Effect of constraints on the equilibrium swelling of rubber vulcanizates. J. Polym. Sci. A Gen. Pap. 3 (2), 641–646.

Suzuki, A., Tanaka, T., 1990. Phase transition in polymer gels induced by visible light. Nature 346, 345.

Sylvester, J.J., 1852. A demonstration of the theorem that every homogeneous quadratic polynomial is reducible by real orthogonal substitutions to the form of a sum of positive and negative squares. Philos. Mag. 4 (23), 138–142.

Takahashi, R., Ikura, Y., King, D.R., Nonoyama, T., Nakajima, T., Kurokawa, T., Kuroda, H., Tonegawa, Y., Gong, J.P., 2016. Coupled instabilities of surface crease and bulk bending during fast free swelling of hydrogels. Soft Matter 12 (23), 5081–5088.

Tanaka, T., 1986. Kinetics of phase transition in polymer gels. Physica A 140 (1), 261–268.

Tanaka, T., Fillmore, D., Sun, S.-T., Nishio, I., Swislow, G., Shah, A., 1980. Phase transitions in ionic gels. Phys. Rev. Lett. 45, 1636–1639.

Tanaka, T., Nishio, I., Sun, S.-T., Ueno-Nishio, S., 1982. Collapse of gels in an electric field. Science 218 (4571), 467–469.

Trujillo, V., Kim, J., Hayward, R.C., 2008. Creasing instability of surface-attached hydrogels. Soft Matter 4 (3), 564–569.

Wang, X., Zhai, Z., Chen, Y., Jiang, H., 2018. A facile, robust and versatile finite element implementation to study the time-dependent behaviors of responsive gels. Extreme Mech. Lett. 22, 89–97.

Weiss, F., Cai, S., Hu, Y., Kang, M.K., Huang, R., Suo, Z., 2013. Creases and wrinkles on the surface of a swollen gel. J. Appl. Phys. 114 (7), 073507.

Wriggers, P., 2008. Nonlinear Finite Element Methods. Springer, Berlin.

Yoon, J., Kim, J., Hayward, R.C., 2010. Nucleation, growth, and hysteresis of surface creases on swelled polymer gels. Soft Matter 6 (22), 5807–5816.

Zorin, D., Schröder, P., 2000. Subdivision for modeling and animation. SIGGRAPH 2000 Course Notes.